Advanced Optical Materials

ADVANCED OPTICAL MATERIALS
www.advopticalmat.de

RESEARCH ARTICLE

Shape-Sensitive Second-Harmonic Generation in Mie-resonant TMDC Nanoparticles

Maria D. Volkova[1,2] | Alena A. Nazarenko[1,2] | Anna A. Popkova[1,2] | Michail Kashchenko[3,4] | Sergey M. Novikov[3] | Anton A. Popov[3,5] | Gleb I. Tselikov[6] | Valentyn S. Volkov[6] | Vladimir O. Bessonov[2] | Andrey A. Fedyanin[2]

[1]Department of Materials Science, Shenzhen MSU-BIT University, Shenzhen, China | [2]Faculty of Physics, Lomonosov Moscow State University, Moscow, Russia | [3]Moscow Center for Advanced Studies, Moscow, Russia | [4]Center for Neurophysics and Neuromorphic Technologies, Moscow, Russia | [5]Institute of Engineering Physics for Biomedicine, MEPhI, Moscow, Russia | [6]Emerging Technologies Research Center, XPANCEO, Dubai, United Arab Emirates

Correspondence: Andrey A. Fedyanin (fedyanin@nanolab.phys.msu.ru)

Received: 5 May 2026 | **Revised:** 20 July 2026 | **Accepted:** 17 August 2026

Keywords: Mie-resonance | molibdenum disulfide | second-harmonic generation | SHG rotational anisotropy | transition metal dichalcogenides

ABSTRACT

The miniaturization and functionality of Mie-tronic devices impose the use of high-index materials with a blueshifted transparency window and high quadratic nonlinearity. In this regard, transition metal dichalcogenides (TMDCs) are promising candidates, which also exhibit excitons at room temperature. In this work, C-exciton-enhanced second-harmonic generation (SHG) in single cylindrical and cubic Mie-resonant nanoparticles made of 2H − MoS_2 flakes is investigated. The study shows that SHG rotational anisotropy (SHG-RA) is sensitive to the geometric shape of nanoparticles. In particular, the rotational patterns from cuboid nanoparticles exhibit considerable two-fold modulation, which is governed by the altering pump field distribution inside the nanoparticle as it rotates relative to the pump polarization direction. A slight deviation from the cube shape results in a strong spectral dependence of rotational patterns when tuning the wavelength through a Mie-driven SHG resonance. These results may be important for designing and optimizing the nonlinear response of TMDC-based metasurfaces.

1 | Introduction

The rapid advancement of nanophotonics is fundamentally driven by the tendency to confine and manipulate light at the subwavelength scale. Dielectric and semiconductor nanoantennas have emerged as pivotal components in this field, capable of supporting high-quality optical resonances with efficient light localization. Mie-type resonances in nanoparticles are of particular interest, offering a versatile platform for on-chip nanolasers, sensors, and nonlinear optical converters [1–5]. In contrast to the plasmonic counterparts [6], dielectric Mie resonators exhibit significantly lower optical losses and can sustain both electric and magnetic resonant modes, providing a rich foundation for engineering a strong linear and nonlinear optical responses [7–11]. In particular, second-harmonic generation (SHG) is sensitive to local electromagnetic field enhancement and increases dramatically when either the fundamental or the harmonic frequency overlaps with a resonant mode of a nanostructure, enabling detectable signals even from individual nanoparticles [12–15]. Beyond second-harmonic (SH) intensity enhancement, recent efforts have also focused on controlling the directional characteristics of the nonlinear emission from individual nanoantennas, as demonstrated for GaAs structures [16, 17]. Therefore, materials with a high refractive index and a large quadratic susceptibility are in demand for use in nonlinear nanophotonics.

Among such materials, transition metal dichalcogenides (TMDCs) have emerged as a particularly promising class due

to their unique electronic and optical properties [18–25]. In their monolayer form, TMDCs exhibit a direct bandgap in the visible and near-infrared range and a lack of inversion symmetry, resulting in a strong second-order nonlinear optical susceptibility [26–33]. The crystal structure of a TMDC monolayer belongs to the D_{3h} point group, which dictates a characteristic six-fold SHG rotational anisotropy (SHG-RA), allowing SHG-RA measurements to reconstruct the crystallographic orientation and to probe valley physics [34–36]. The bulk TMDCs retain the exciton response of monolayers, possessing a blueshifted transparency window and a higher refractive index compared to silicon. Being a centrosymmetric material, bulk TMDC in hexagonal phase (2H) should not exhibit second-order nonlinear effects in the volume in the dipole approximation, while demonstrating a near-surface SHG response, as well as a quadrupole contribution in the spectral region of the material resonances, such as excitons [37, 38]. These effects can be significantly increased in Mie-resonant structures due to the strong electromagnetic field localization in the vicinity of the SH sources' location. Thus, maximum amplification of the nonlinear response is achieved if the pump wavelength is adjusted to excite the Mie resonance, and the harmonic wavelength is tailored to the spectral position of the exciton resonance of the material [13, 39, 40].

The SHG response is determined by the second-order nonlinear susceptibility tensor $\chi^{(2)}$ and the distribution of electromagnetic fields inside the structure, which in turn is defined by the type of resonances excited. Therefore, SHG-RA dependences of Mie-resonant structures should depend on both the nonlinear material and the geometry of the nanoresonators. In this work, a comparative experimental study of the SHG-RA response of molybdenum disulfide (MoS_2) nanoantennas supporting Mie resonances in the near-infrared spectral range is presented. Two distinct nanoantenna shapes are investigated: cuboid and cylinder. The obtained results reveal a fundamental difference in the origin of the measured SHG anisotropic patterns. For cylindrical nanoantennas, the SHG-RA dependence is found to be predominantly governed by the symmetry of the bulk nonlinear susceptibility tensor of the crystalline material. In contrast, the symmetry of the nanocuboid's Mie modes themselves plays a defining role, significantly reshaping the SHG-RA response. These findings provide new insights into nanoscale nonlinear optics, highlighting how the dominant factor in SHG-RA measurements can transition from material symmetry to resonant mode symmetry based on geometry, with implications for the design of nonlinear metasurfaces and integrated photonic devices.

2 | Results and Discussion

The schematic illustration of the system is presented in Figure 1a. The sample under study was a set of individual subwavelength-sized nanoresonators located at a two-layer SiO_2/Si substrate. Two geometries of nanoresonators are cylinders and cuboids with dimensions of approximately four hundred nanometers. The nanoparticle size was chosen to be sufficiently large so that multiple Mie modes could be excited in the pump spectral region near the doubled wavelength of the C-exciton, thereby allowing the quadratic susceptibility resonance to be utilized [13, 27]. The resulting high-order Mie modes exhibit sharp features in the electric field distribution that can be localized near the nanoparticle surface. Since the absorption coefficient of MoS_2 at the C-exciton wavelength is about 0.1 nm^{-1} [25] (penetration depth ≈ 10 nm), the SH signal originates from the top surface layer of the structure. The localization of the electric field on the top surface therefore not only enhances the SH signal under these strong absorption conditions but also ensures high sensitivity to small changes in geometric shape and pump wavelength.

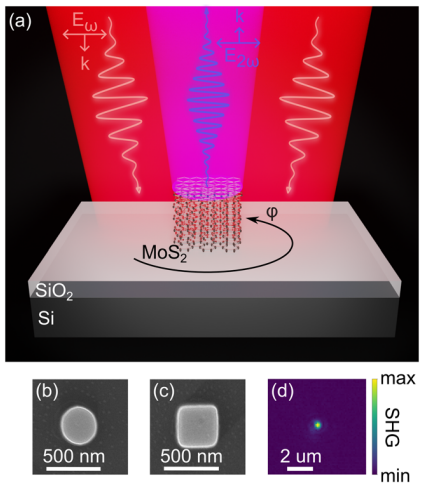

FIGURE 1 | (a) Schematic of the SHG experiment. (b,c) Scanning electron microscope images of cylindrical (b) and cuboid (c) nanoparticles. (d) SH image of a single cubic nanoparticle.

The structures were fabricated from single-crystal 2H – MoS_2 flakes by electron-beam lithography followed by reactive ion etching (see Section S1). The sizes of the structures were verified using scanning electron microscopy (SEM) (Figure 1b,c) and atomic force microscopy (AFM) (Figure S1a) measurements. The height of nanoparticles was 400 nm, the radius of the cylinders was 215 nm, while the side length of the cuboids was 380 nm. More accurate values of the geometrical parameters were obtained by comparing the results of numerical simulation with experimental data. The simulation revealed that the cube sides in the horizontal cross-section are not equal and differ from each other by about 5%.

The SH signal was obtained using a home-built multiphoton microscope specially designed for measuring optical harmonics in a reflection configuration. The light source was a femtosecond laser (Coherent Chameleon) tunable in the spectral range from 680 to 1080 nm. This spectral region corresponds to the transparency of MoS_2 and covers wavelengths that are twice that of the C-exciton [13, 27]. As the SH signal is generated by the first 10–15 nm of material, the effect of the even or odd number of MoS_2 layers is not observed in the wavelength range under study. The sample was illuminated by a slightly focused pump beam with a diameter of 10 um at normal incidence on the sample surface, thus providing near-plane-wave illumination. The SHG image collected from the pumped area was captured with a CMOS (Photometrics Prime) camera. This allowed the SH signal to be detected only from particles as shown in Figure 1c. The image is a bright area corresponding to a solitary nanoparticle. The signal from the substrate is several orders of magnitude smaller than

the signal from the particle at resonant wavelengths. The SH intensity from the nanoresonator was obtained by integrating the signals from the individual pixels within the sample region of the image. For detailed information see Supporting Information in Ref. [13]. The SH intensity of the sample as a function of pump wavelength was measured by tuning the pump wavelength, while keeping the pump power constant. The experimental scattering spectra were obtained by placing a block in the detection channel to suppress the central region of the back focal plane image, through which the beam mirrored from the substrate passes. To measure the rotational anisotropy of the second harmonic generation (SHG-RA), the sample was rotated around the optical axis while the polarization of the pump radiation remained fixed. The reflected SH intensity as a function of the azimuthal angle φ relative to the incident polarization direction was measured. The zero azimuthal angle was defined by the alignment of the pump polarization direction with the longest dimension of the cuboid. For polarization-resolved measurements, an analyzer was additionally placed in the detection channel, the orientation of which was parallel or perpendicular to the polarization of the pump radiation.

Numerical calculations of linear and nonlinear response were performed in COMSOL Multiphysics software by the finite element method (FEM). MoS_2 nanoresonators were simulated on a multilayered SiO_2/Sisubstrate with a 290-nm-thick SiO_2 layer. The cuboid model had dimensions of 375 nm (width), 390 nm (length), and 400 nm (height). The radius of the cylinder was 215 nm and its height was 400 nm. The simulation area was bounded in all directions by perfectly matched layers (see details in Section S2). The multipole decomposition of the scattering cross-section (SCS) was conducted using the semianalytical formula described in Ref.[41]. The refractive indices and the absorption coefficients of the MoS_2, Si and SiO_2 were taken from the literature [25, 42, 43]. In the nonlinear simulation (see Section S4), the second-order nonlinear susceptibility spectrum was taken in the form of a Lorentzian function with a central wavelength of 885 nm [27] and a FWHM of 50 nm (typical for MoS_2 [44]), while the symmetry properties of $2H-MoS_2$ corresponded to the monolayer ones [26]. The calculation of SHG-RA was performed by rotating the studied nanostructure relative to the laboratory coordinate system with a fixed pump polarization. The nonlinear response of the system is determined both by the rotation of the structure itself and by the orientation of the MoS_2 crystal axes relative to the structure's sides. In the case of cuboids, the angle between the crystal axis and the long side was determined experimentally from the polarization-resolved SHG-RA dependences and amounted to 40°.

Mie-type resonances excited in the nanoparticles manifest themselves as features in the scattering spectra. Figure 2a,c (dots) display the experimental scattering spectra of the MoS_2 cylinder and cuboid, respectively, for pump polarization along the long side of the cuboid. The scattering cross-section spectra were also calculated (Figure 2a,c, curves) to determine the influence of excited Mie resonances on the linear optical response. The SCS spectra for the orthogonal pump polarization (along the short side of the cuboid) exhibit similar behavior and are presented in Section S5. The main multipoles contributing to the SCS spectra in the laser spectral range are presented in Figure 2b,d (a broad spectral range is shown in the Section S2). The measured and calculated results demonstrate good agreement in the spectral shapes and the positions of the resonances. Due to the large size of the nanostructures, all of the first four multipoles make a significant contribution to SCS and spatial distribution of the pump field inside the cuboid in the studied range.

At the start of the nonlinear measurements, we proved that the entire detected signal was SH radiation, with no luminescence present (see Section S3). The spectral dependences of the SH power for the MoS_2 cylinder and cuboid, measured by tuning the pump wavelength with the polarization along the long side of the cuboid, are presented in Figure 3a. The corresponding calculation results (Figure 3b) demonstrate good agreement with experimental ones. The curves for both cylinder and cuboid show the presence of three peaks with various amplitudes. For the cuboid, the maximum SH power is observed at 830 nm. For the cylinder, the peak position is 960 nm and corresponds to the position of the second SHG peak of the cuboid. The amplitude of the SH signal at 960 nm is similar for both nanoparticles. At the resonances, the intensity of SHG from nanostructures exceeds that from the MoS_2 flake and monolayer by an order of magnitude (see Figure S4). Note that not all resonances observed in the scattering spectra lead to resonances in the SHG spectra. Strong absorption at the SH frequency means that only the uppermost 10-nm-thick layer of the nanoparticle contributes to the detectable SH signal. Therefore, SH is effectively generated only by pump modes whose electric field is partially concentrated at the top of the nanoparticle, and these modes also determine the SH radiation direction (for detailed information, see Section S4). As a result, the positions of the SHG peaks do not have to coincide with the positions of the scattering peaks. Consequently, based solely on scattering spectra and multipole decomposition in such structures, it is difficult to predict the behavior of the SHG response, and rigorous calculations of nonlinear response are required.

To investigate the interplay between the crystal lattice symmetry and the nanoresonator's shape in the SHG process, the SHG-RA measurements were carried out. The experimentally and numerically obtained SH intensity dependences on the azimuthal angle φ for the MoS_2 cylinder and cuboid are presented in Figure 4a,b. The green curves indicate the measurements without an analyzer (polarization-unresolved), while the blue curves correspond to the parallel orientation of the SH and pump polarizations. The polarization-unresolved SHG-RA for the cylinder demonstrates an almost constant SH intensity for all azimuthal angles φ. Small deviations of the experimental curve from the constant value may be a consequence of the slight ellipticity of the cylinder shape. The polarization-resolved measurements demonstrate six pronounced peaks, in accordance with the D_{3h} symmetry of monolayer MoS_2 crystal lattice. A similar behavior has been observed in previous studies of SHG anisotropy from MoS_2 monolayers [26–28], $2H-MoS_2$ thin films [26, 37] and nanodisks [13]. Therefore, the infinite rotational symmetry of the cylinder does not contribute to the SHG-RA. In the case of the cuboid, the polarization-unresolved rotational pattern exhibits a two-fold symmetry. This is consistent with the two-fold symmetry of the rectangle in the horizontal cross-section of the cuboid, despite the slight difference in side length. For the square cross-section, unpolarized SHG has a four-fold anisotropic response as shown by numerical calculations (Figure S7). Therefore, even

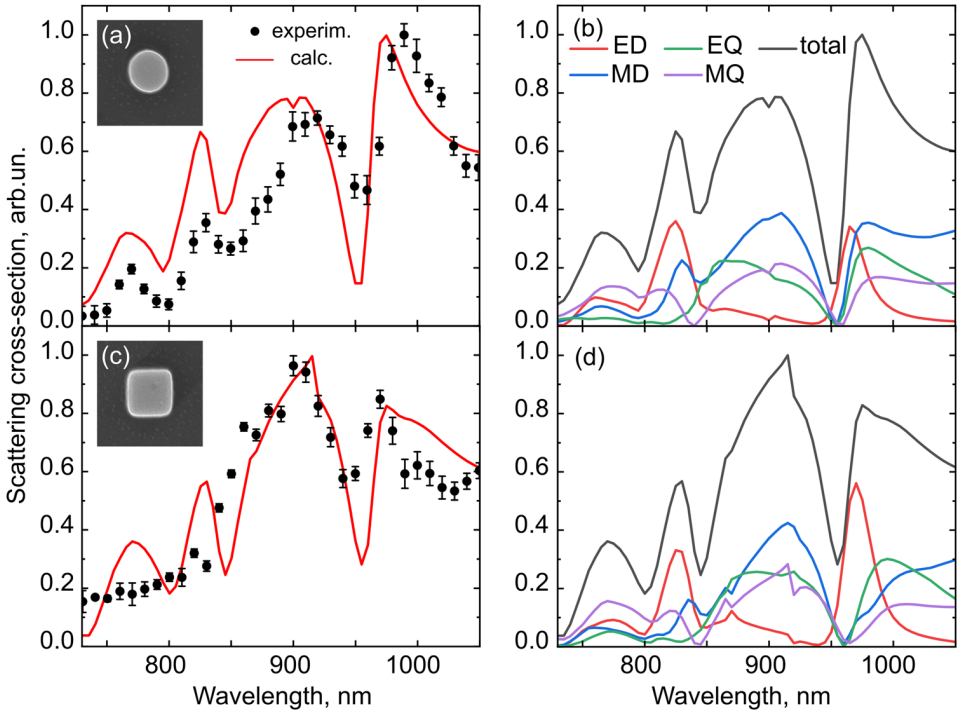

FIGURE 2 | Measured (dots) and calculated (curves) scattering spectra of the cylinder (a) and cuboid (c), along with the results of their multipole decomposition (b,d). ED – electric dipole mode, MD – magnetic dipole mode, EQ – electric quadrupole mode, MQ – magnetic quadrupole mode.

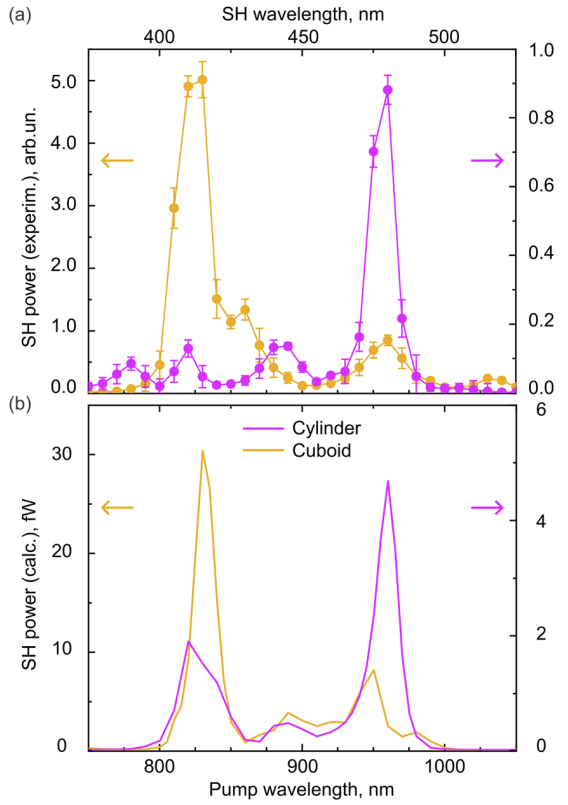

FIGURE 3 | (a,b) Experimental (dots) and calculated (solid curves) SH power dependences on the pump wavelength for the cylindrical (magenta curve) and cubic (yellow curve) MoS_2 nanoparticles. The pump polarization direction is parallel to the long side of the cuboid. The results are obtained for unpolarized SH radiation.

slight breaks in nanoparticle symmetry are captured by SHG-RA patterns. Note that the unpolarized SHG pattern is sufficient for assessing the symmetry of the structure under investigation. The polarized SH rotational pattern from the cuboid exhibits six-fold crystalline symmetry. However, the amplitude of the peaks is affected by the cuboid's two-fold symmetry. Unpolarized SHG anisotropy occurs due to a change in the configuration of the pump field inside the cuboid as it rotates relative to the pump polarization direction (see Section S7). In this case, the pump field intensity in the cuboid's near-surface layer can vary significantly, resulting in the SH intensity changing by an order of magnitude for different orientations of the cuboid.

The local electromagnetic field distribution also depends strongly on the pump wavelength due to the excitation of multiple Mie-type resonances within the spectral range under study. Consequently, tuning the pump wavelength should induce a pronounced modification of the SHG anisotropy pattern, especially near the resonances of the nonlinear response. Figure 5a,b shows the SHG-RA patterns measured for the cuboid at two close pump wavelengths of 810 and 820 nm near the largest SHG resonance peak. Green curves correspond to the polarization-unresolved SHG-RA measurements, blue and violet curves are related to the parallel and perpendicular mutual orientations of the SH and pump polarization directions, respectively. The unpolarized SH patterns demonstrate two-fold symmetry for both pump wavelengths. However, the direction of the SH intensity maximum rotates by approximately 90° as the wavelength changes. This observation directly demonstrates the connection between SHG rotational patterns and the wavelength- and polarization-dependent distribution of the pump electric field inside the cuboid. The observed behavior of anisotropic dependences was numerically simulated by carefully selecting the cuboid

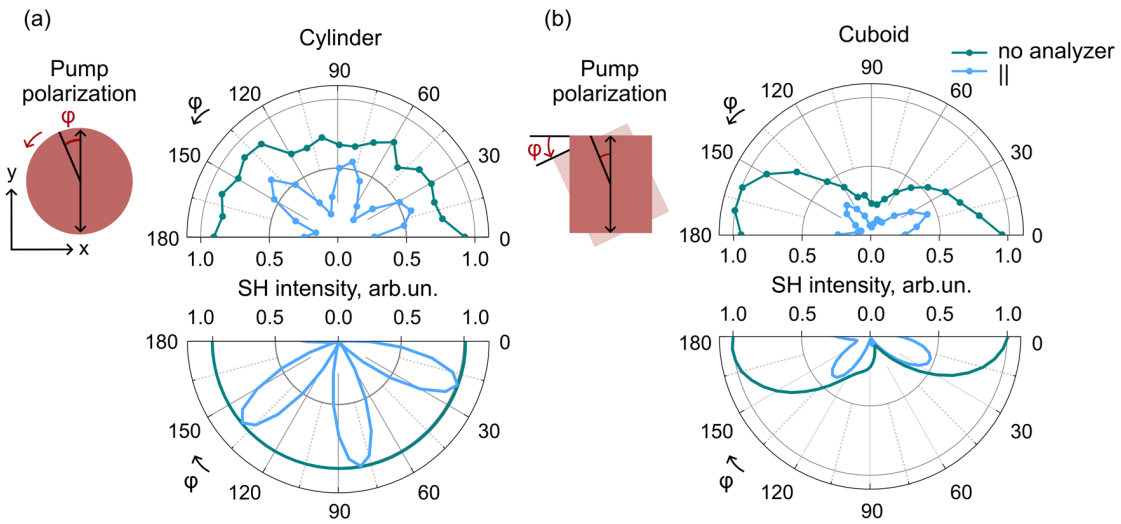

FIGURE 4 | (a,b) The measured (dots)and calculated (solid curves) SH intensity dependences on the azimuthal angle φ for the cylinder (a) and cuboid (b) nanoparticles. Green curves are related to the unpolarized SH radiation. Blue curves correspond to the parallel orientation of the SH and pump radiation polarization. The results for the cylinder and cuboid were obtained at pump wavelengths of 960 and 920 nm, respectively. The zero azimuthal angle corresponds to the alignment of the pump polarization direction with the longest dimension of the cuboid.

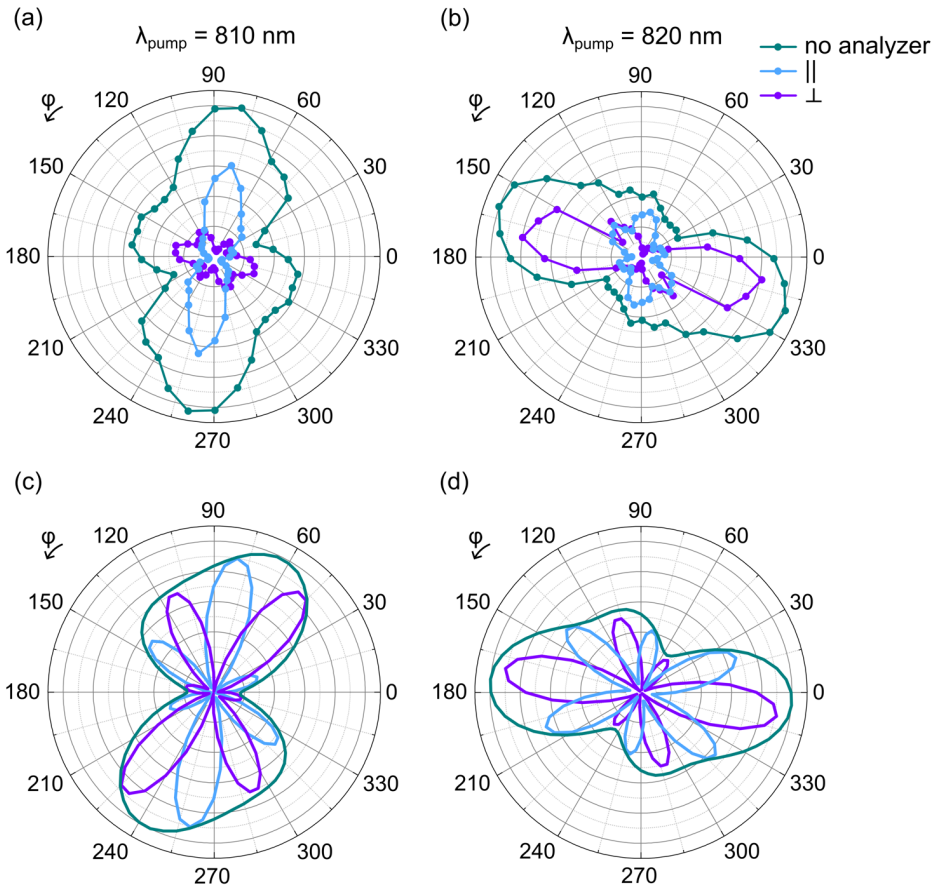

FIGURE 5 | The measured (a,b) and calculated (c,d) SH intensity dependences on the azimuthal angle φ of the cuboid rotation at close pump wavelengths. Green curves correspond to the polarization-unresolved SH intensity measurements. Blue and violet curves correspond to the parallel and perpendicular orientation of the SH and pump radiation polarization, respectively.

parameters (Figure 5c,d). This effect is also analyzed qualitatively by calculating the spatial field distributions within the top layer of the MoS_2 cuboid at two excitation wavelengths and for different azimuthal angles (see Section S7). The calculations show that even at close wavelengths the modes excited inside the cuboid are quite different. At the same time, due to the different lengths of the cuboid's sides, the modes also differ for the cases where the polarization of the pump field is aligned along the long and short sides of the cuboid (i.e., for $\varphi = 0°$ and $\varphi = 90°$). For the short wavelength, the pump field has a higher intensity at $\varphi = 90°$ than at $\varphi = 0°$. As a result, the lobes of the SHG-RA pattern are oriented predominantly at the $\varphi = 90°$ direction. For the long wavelength, the highest intensity of the pump field is observed at $\varphi = 0°$, i.e., when the polarization of the pump field is aligned along the long side of the cube. In this case, the lobes of the SHG-RA pattern are oriented predominantly along the $\varphi = 0°$ direction.

The polarization-resolved SH intensity dependences in Figure 5 demonstrate six peaks of different amplitudes, corresponding to the crystal lattice contribution to the anisotropy pattern. The directions of these maxima remain unchanged with the tuning of the pump wavelength due to their association with the MoS_2 crystallographic axes. Depending on the type of excited Mie mode, the maximum of the polarized SHG is observed in either the parallel or the perpendicular component of the SH signal. Thus, the dependence of the SHG response on the excited Mie mode type in the MoS_2 cuboid can be used to tune the SHG efficiency. Moreover, the pronounced sensitivity of the nonlinear optical response to the local field distribution implies that even minor geometric variations in the resonator shape are dramatically amplified in the SHG-RA patterns. In the case of a cuboid, deviations of less than 5% from a square shape change the symmetry of the observed dependences (see Section S6). This extreme structural sensitivity, which is inherently more pronounced in the nonlinear regime than in its linear counterpart, suggests that SHG-RA measurements can serve as an ultrasensitive probe for quantifying nanoscale morphological deviations, offering a non-invasive optical metrology tool for the quality control of fabricated nanostructures.

3 | Conclusion

In conclusion, we have investigated the anisotropic SHG response in the MoS_2 nanoantennas with cylindrical and cuboid shapes in the near-infrared spectral range of the pump radiation corresponding to the C-exciton spectral range of the SH radiation. Because of the infinite rotational symmetry of the cylinder, the unpolarized SH intensity as a function of the azimuthal angle of sample rotation is almost unchanged, as in the case of the MoS_2 monolayer and thin films. The polarization-resolved SHG anisotropy of the cylinder is governed by the MoS_2 crystal symmetry. For the cuboid, the SHG-RA dependences exhibit qualitatively different behavior. The finite rotational symmetry of the cuboid leads to a corresponding modification of the electric field distribution when the cuboid rotates. Consequently, the Mie-modes altering during rotation strongly affect the SHG anisotropy pattern of the MoS_2 cuboid. As a result, the unpolarized SHG-RA patterns are largely governed by the symmetry of the nanoparticle, and in particular by the configuration of the excited modes. The crystal lattice contribution to the polarization-resolved SHG response is in turn modulated by the Mie resonances excited within the structure. This interplay between the excited mode configuration and the crystal lattice symmetry enables the nonlinear optical response to be tailored by changing the type of the excited mode, for example, by adjusting the excitation wavelength. The type of the nonlinear susceptibility tensor of MoS_2 also allows one to additionally switch between the minimum and maximum of the nonlinear signal when changing the direction of the detected SHG component. In addition, the ability of the nonlinear response to amplify minor structural variations – an effect far less prominent in linear measurements – makes the SHG-RA method an exceptional candidate for quantifying slight shape deviations. This approach thus provides a non-invasive optical assay for assessing the structural fidelity of nanophotonic devices. Moreover, the observed interplay between crystal symmetry and resonator geometry offers a route to actively tailor the nonlinear anisotropy of TMDC-based metasurfaces, which is essential for applications such as polarization-sensitive frequency conversion, optical routing, and on-chip nonlinear signal processing.

Acknowledgements

The work was performed under financial support of Russian Science Foundation (grant No. 24-19-00478). The study was conducted under the state assignment of Lomonosov Moscow State University and was funded by Shenzhen Municipal Government and Shenzhen MSU-BIT University. A.A.N. acknowledges the Foundation for the Advancement of Theoretical Physics and Mathematics "BASIS" for the scholarship award. S.M.N. thanks the Ministry of Science and Higher Education of the Russian Federation (FSMG-2024-0014).

Conflicts of Interest

The authors declare no conflicts of interest.

Data Availability Statement

The data that support the findings of this study are available from the corresponding author upon reasonable request.

References

1. A. I. Kuznetsov, A. E. Miroshnichenko, M. L. Brongersma, Y. S. Kivshar, and B. Luk'yanchuk, "Optically Resonant Dielectric Nanostructures," *Science* 354, no. 6314 (2016): aag2472.

2. S. Kruk and Y. Kivshar, "Functional Meta-Optics And Nanophotonics Governed By Mie Resonances," *ACS Photonics* 4, no. 11 (2017): 2638–2649.

3. E. Tiguntseva, K. Koshelev, A. Furasova, et al., "Room-Temperature Lasing From Mie-Resonant Nonplasmonic Nanoparticles," *ACS Nano* 14, no. 7 (2020): 8149–8156.

4. M. Rakhlin, T. V. Antipov, A. D. Gartman, et al., "Mie-Resonant Silicon Waveguide For Efficient Coupling With Excitonic Emitters in InSe," *Journal of Materials Chemistry C* 14, no. 1 (2026): 336–342.

5. V. E. Babicheva and A. B. Evlyukhin, "Mie-Resonant Metaphotonics," *Advances in Optics and Photonics* 16, no. 3 (2024): 539–658.

6. J. Olson, S. Dominguez-Medina, A. Hoggard, L.-Y. Wang, W.-S. Chang, and S. Link, "Optical Characterization Of Single Plasmonic Nanoparticles," *Chemical Society Reviews* 44, no. 1 (2015): 40–57.

7. M. R. Shcherbakov, D. N. Neshev, B. Hopkins, et al., "Enhanced Third-Harmonic Generation In Silicon Nanoparticles Driven By Magnetic Response," *Nano Letters* 14, no. 11 (2014): 6488–6492.

8. M. K. Kroychuk, D. F. Yagudin, A. S. Shorokhov, et al., "Tailored Nonlinear Anisotropy In Mie-Resonant Dielectric Oligomers," *Advanced Optical Materials* 7, no. 20 (2019): 1900447.

9. F. Timpu, J. Sendra, C. Renaut, et al., "Lithium Niobate Nanocubes As Linear And Nonlinear Ultraviolet Mie Resonators," *ACS Photonics* 6, no. 2 (2019): 545–552.

10. T. Hinamoto, M. Hamada, H. Sugimoto, and M. Fujii, "Angle-, Polarization-, And Wavelength-Resolved Light Scattering Of Single Mie Resonators Using Fourier-Plane Spectroscopy," *Advanced Optical Materials* 9, no. 8 (2021): 2002192.

11. Z. Lu, K. Koshelev, P. Tonkaev, et al., "Light–Matter Interaction In Van Der Waals Heterostructures With Mie Voids," *Advanced Photonics* 8, no. 2 (2026): 026002–026002.

12. K. Koshelev, S. Kruk, E. Melik-Gaykazyan, et al., "Subwavelength Dielectric Resonators For Nonlinear Nanophotonics," *Science* 367, no. 6475 (2020): 288–292.

13. A. A. Popkova, I. M. Antropov, G. I. Tselikov, et al., "Nonlinear Exciton-Mie Coupling In Transition Metal Dichalcogenide Nanoresonators," *Laser and Photonics Reviews* 16, no. 6 (2022): 2100604.

14. D. M. Zhigunov, D. A. Shilkin, V. O. Bessonov, et al., "Linear and Nonlinear Optical Response of Mie-Resonant Si Nanoparticles And Its Modification Induced By Femtosecond Irradiation Post-Treatment," *Optical Materials* 154 (2024): 115616.

15. R. Biswas, A. Prosad, A. S. Lal Krishna, et al., "Leveraging Strong Electric Field Gradients At Anapole Resonances For Enhanced Second Harmonic Generation From Molybdenum Disulfide Disks," *Advanced Materials* 37, no. 14 (2025): 2418257.

16. L. Xu, G. Saerens, M. Timofeeva, et al., "Forward and Backward Switching Of Nonlinear Unidirectional Emission From GaAs Nanoantennas," *ACS Nano* 14, no. 2 (2019): 1379–1389.

17. J. D. Sautter, L. Xu, A. E. Miroshnichenko, et al., "Tailoring Second-Harmonic Emission From (111)-GaAs Nanoantennas," *Nano Letters* 19, no. 6 (2019): 3905–3911.

18. K. F. Mak, C. Lee, J. Hone, J. Shan, and T. F. Heinz, "Atomically Thin MoS_2: A New Direct-Gap Semiconductor," *Physical Review Letters* 105, no. 13 (2010): 136805.

19. A. Splendiani, L. Sun, Y. Zhang, et al., "Emerging Photoluminescence In Monolayer MoS_2," *Nano Letters* 10, no. 4 (2010): 1271–1275.

20. A. Kuc, N. Zibouche, and T. Heine, "Influence of Quantum Confinement On The Electronic Structure Of The Transition Metal Sulfide TS_2," *Physical Review B* 83, no. 24 (2011): 245213.

21. Q. H. Wang, K. Kalantar-Zadeh, A. Kis, J. N. Coleman, and M. S. Strano, "Electronics and Optoelectronics Of Two-Dimensional Transition Metal Dichalcogenides," *Nature Nanotechnology* 7, no. 11 (2012): 699–712.

22. D. Y. Qiu, F. H. Da Jornada, and S. G. Louie, "Optical Spectrum Of MoS_2: Many-Body Effects And Diversity Of Exciton States," *Physical Review Letters* 111, no. 21 (2013): 216805.

23. A. Gupta, T. Sakthivel, and S. Seal, "Recent Development In 2D Materials Beyond Graphene," *Progress in Materials Science* 73 (2015): 44–126.

24. A. Castellanos-Gomez, J. Quereda, H. P. van der Meulen, N. Agraït, and G. Rubio-Bollinger, "Spatially Resolved Optical Absorption Spectroscopy Of Single-and Few-Layer MoS_2 by Hyperspectral Imaging," *Nanotechnology* 27, no. 11 (2016): 115705.

25. G. Ermolaev, D. Grudinin, Y. Stebunov, et al., "Giant Optical Anisotropy In Transition Metal Dichalcogenides For Next-Generation Photonics," *Nature Communications* 12, no. 1 (2021): 854.

26. N. Kumar, S. Najmaei, Q. Cui, et al., "Second Harmonic Microscopy Of Monolayer MoS_2," *Physical Review B* 87, no. 16 (2013): 161403.

27. L. M. Malard, T. V. Alencar, A. P. M. Barboza, K. F. Mak, and A. M. de Paula, "Observation of Intense Second Harmonic Generation From MoS_2 Atomic Crystals," *Physical Review B* 87 (May 2013): 201401.

28. Y. Li, Y. Rao, K. F. Mak,, et al., "Probing Symmetry Properties Of Few-Layer MoS_2 and H-BN By Optical Second-Harmonic Generation," *Nano Letters* 13, no. 7 (2013): 3329–3333.

29. D. Clark, V. Senthilkumar, C. Le, et al., "Strong Optical Nonlinearity of CVD-Grown MoS_2 Monolayer As Probed By Wavelength-Dependent Second-Harmonic Generation," *Physical Review B* 90, no. 12 (2014): 121409.

30. A. Autere, H. Jussila, A. Marini, et al., "Optical Harmonic Generation In Monolayer Group-VI Transition Metal Dichalcogenides," *Physical Review B* 98, no. 11 (2018): 115426.

31. W. Liu, M. Liu, X. Liu, et al., "Recent Advances Of 2D Materials In Nonlinear Photonics and Fiber Lasers," *Advanced Optical Materials* 8, no. 8 (2020): 1901631.

32. A. A. Nazarenko, A. M. Chernyak, A. I. Musorin, et al., "Cryogenic Nonlinear Microscopy Of High-Q Metasurfaces Coupled With Transition Metal Dichalcogenide Monolayers," *Nanophotonics* 13, no. 18 (2024): 3429–3436.

33. L. Seidt, T. Weber, A. A. Seredin, et al., "Ultrafast All-Optical Switching In Nonlinear 3R-MoS_2 Van Der Waals Metasurfaces," *npj Nanophotonics* 2, no. 1 (2025): 37.

34. G. M. Maragkakis, S. Psilodimitrakopoulos, L. Mouchliadis, et al., "Imaging the Crystal Orientation Of 2D Transition Metal Dichalcogenides Using Polarization-Resolved Second-Harmonic Generation," *Opto-Electronic Advances* 2, no. 11 (2019): 190026–1.

35. H. Hu, K. Wang, H. Long, W. Liu, B. Wang, and P. Lu, "Precise Determination Of the Crystallographic Orientations In Single ZnS Nanowires By Second-Harmonic Generation Microscopy," *Nano Letters* 15, no. 5 (2015): 3351–3357.

36. J. J. Dean and H. M. van Driel, "Graphene and Few-Layer Graphite Probed By Second-Harmonic Generation: Theory and Experiment," *Physical Review B* 82, no. 12 (2010): 125411.

37. S. Shree, D. Lagarde, L. Lombez, et al., "Interlayer Exciton Mediated Second Harmonic Generation In Bilayer MoS_2," *Nature Communications* 12, no. 1 (2021): 6894.

38. J. Klein, J. Wierzbowski, A. Steinhoff, et al., "Electric-Field Switchable Second-Harmonic Generation In Bilayer MoS_2 By Inversion Symmetry Breaking," *Nano Letters* 17, no. 1 (2017): 392–398.

39. M. Nauman, J. Yan, D. de Ceglia, et al., "Tunable Unidirectional Nonlinear Emission From Transition-Metal-Dichalcogenide Metasurfaces," *Nature Communications* 12, no. 1 (2021): 5597.

40. M. Nauman, D. De Ceglia, J. Yan, et al., "Dynamic Control of Nonlinear Emission By Exciton-Photon Coupling in WS_2," *Science Advances* 11, no. 35 (2025): eady2108.

41. A. B. Evlyukhin and B. N. Chichkov, "Multipole Decompositions For Directional Light Scattering," *Physical Review B* 100, no. 12 (2019): 125415.

42. E. D. Palik, *Handbook of Optical Constants of Solids*, Vol. 3 (Academic Press, 1998).

43. C. Schinke, P. Christian Peest, J. Schmidt, et al., "Uncertainty Analysis For The Coefficient Of Band-To-Band Absorption of Crystalline Silicon," *AIP Advances* 5, no. 6 (2015): 067168.

44. L. Lafeta, A. Corradi, T. Zhang, et al., "Second-and Third-Order Optical Susceptibilities Across Excitons States In 2D Monolayer Transition Metal Dichalcogenides," *2D Materials* 8, no. 3 (2021): 035010.

Supporting Information

Additional supporting information can be found online in the Supporting Information section.

Supporting File: adom71705-sup-0001-SuppMat.pdf.